https://doi.org/10.5194/egusphere-2026-2911
Preprint. Discussion started: 30 June 2026

Rethinking fractal scaling of sea ice deformation: the dominant role of signed-gradient cancellation

Florence L. Beaudry[1] and L. Bruno Tremblay[1]

[1]Department of Atmospheric and Oceanic Sciences, McGill University, Montréal, Québec, Canada

Correspondence: Florence L. Beaudry (florence.beaudry@mail.mcgill.ca)

Abstract. We use synthetic sea ice velocity fields to assess the robustness and physical interpretation of first-order scaling diagnostics, commonly associated with spatial localization in the sea ice modeling community. The synthetic fields are constructed to reproduce a wide range of RADARSAT Geophysical Processor System (RGPS)-derived deformation statistics while providing full control over signal-to-noise ratio, divergence-to-shear ratio, lead density, orientation and spatial localization. Results show that spatial scaling arises from the cancellation of signed velocity gradients in the coarse-graining procedure rather than from localization. For instance, dirac-delta deformation field mimicking idealized fracture lines does not show scaling in the absence of signed-gradient cancellation, and smoothly varying (non-localized) deformation fields yield scaling exponents comparable to observations when they contain both positive and negative velocity gradients. We further demonstrate that the standard fractal diagnostic is not invariant under rotation: a pure shear (non-divergent) deformation field exhibits different scale dependence when expressed in a rotated frame. These conclusions derived from synthetic deformation fields when applied to real sea ice deformation from RGPS and sea ice models from the Sea Ice Rheology Experiment (SIREx) show that observed scaling is similarly dominated by cancellation between positive and negative strain rates rather than geometric localization, and therefore are largely determined by PDFs of deformations. These findings reveal key limitations in current scale-invariance-derived diagnostics and call for physically interpretable and robust metrics.

1 Introduction

Early sea ice model evaluation focused on large-scale diagnostics such as sea ice drift, extent, and thickness, and comparison with in-situ buoy-derived drifts, submarine-derived ice thickness, and passive microwave remote sensing (e.g., Hibler 1979; Shy et al. 2000; Kreyscher et al. 2000; Ip et al. 1991; Zhang and Rothrock 2005). Any model that incorporated both shear and compressive strength however reproduced these observed bulk properties (Ungermann et al., 2017; Notz et al., 2016). More recently, high-resolution active radar remote sensing data (e.g., RADARSAT, RCM, Sentinel) have permitted the study of sea ice deformations localized along narrow, intermittent linear bands known as Linear Kinematic Features (LKFs; Kwok 2001). Since both shear and divergence are present along LKFs, they are tightly linked to thermodynamic and dynamic processes, and thus to sea ice mass balance and ocean-ice-atmosphere exchanges of heat, moisture, and salt, with important implications for climate and seasonal forecasting (McPhee et al., 2005; Bourgault et al., 2020; Tian et al., 2025). Deformation rates derived from high-resolution RADARSAT imagery show that these features exhibit self-affine, fractal-like structures (Stern et al., 1995;

https://doi.org/10.5194/egusphere-2026-2911
Preprint. Discussion started: 30 June 2026

Coon et al., 1998); i.e., the deformation patterns repeat across a wide range of scales with a preferred direction (Mandelbrot and Wheeler, 1983; Mandelbrot, 1985). This organization is mathematically characterized by power-law scaling relationships (Feder, 1988; Halley et al., 2004; Hamburger et al., 1996). Evidence of scale invariance in sea ice deformation, fracture, and fragmentation emerges through multiple avenues, including power-law distributions of floe size and deformation, box-counting analyses of SAR backscatter, power spectra of buoy dispersion, and structure functions of mean total strain rates (e.g., Rothrock and Thorndike 1984; Martin and Thorndike 1985; Weiss 2001a, b; Weiss and Marsan 2004; Marsan et al. 2004; Hutchings et al. 2011).

The most widely used fractal method in the field of sea ice kinematics involves computing first-order structure functions on strain rate fields obtained via coarse-graining of velocity gradients (Marsan et al., 2004). The resulting spatial scaling exponent β was initially interpreted as a measure of self-organization, or correlation between mean total deformation rates and scales (Weiss and Marsan, 2004; Marsan et al., 2004; Stern and Lindsay, 2009). Later, this same scaling exponent was re-interpreted as a proxy for localization of deformation, where $\beta \sim 0$ implies homogeneous deformation and $\beta \sim 2$ implies strong localization (e.g., Rampal et al. 2008; Marsan and Weiss 2010; Rampal et al. 2019; Bouchat and Tremblay 2017; Bouchat et al. 2022b). Observed values of β typically range between $\sim$0.1 and $\sim$0.8 (Marsan et al., 2004; Rampal et al., 2008; Stern and Lindsay, 2009; Girard et al., 2009; Spreen et al., 2017; Oikkonen et al., 2017; Hutchings et al., 2011; Hutter et al., 2018; Lei et al., 2021; Uusinoka et al., 2025a). The scaling exponent β varies temporally with ice strength (weaker and/or younger ice results in larger scaling exponents; Stern and Lindsay 2009; Hutter et al. 2018; Lei et al. 2021), is sensitive not only to signal-to-noise ratio in the RADARSAT-derived velocity gradients, but also to seemingly minor methodological differences in deformation and scaling exponent retrieval that are regarded as inconsequential, yet significantly affect the scaling exponent (Bouillon and Rampal, 2015b; Bouchat and Tremblay, 2020). Finally, studies using higher-resolution deformation rates from buoys and marine radar show that power-law scaling breaks down at both small and large scales (Hutchings et al., 2024; Uusinoka et al., 2025b, a).

While these scaling exponents have become a standard diagnostic for evaluating the rheological component of sea ice models (Bouillon and Rampal, 2015a; Dansereau et al., 2016; Rampal et al., 2019; Hutter et al., 2018; Bouchat and Tremblay, 2017; Bouchat et al., 2022b; Savard and Tremblay, 2024; Lemieux et al., 2025), their interpretation is not always straightforward. To the best of our knowledge, there is no consensus on their physical interpretation (scale invariant vs. localization). All models, regardless of the underlying physics, can reproduce observed scaling if their spatial resolution is sufficiently high (Bouchat et al., 2022b). For instance, Bouchat and Tremblay (2017) showed that increasing shear strength or reducing compressive strength in low-resolution viscous plastic models increases localization and yields scaling exponents within the observed range, despite the model underestimating LKF density, highlighting the limits of scaling for rheology discrimination. Other studies report on strong sensitivity of scaling exponents to signal-to-noise ratio, with efforts to up-weight large deformation that increases scaling (Bouillon and Rampal, 2015b; Bouchat and Tremblay, 2020). Finally, models with the correct scaling still do not capture key geometric features, such as observed LKF intersection angles and density (Hutter and Losch, 2020; Hutter et al., 2022), prompting a reassessment of the physical meaning of *scaling*.

https://doi.org/10.5194/egusphere-2026-2911
Preprint. Discussion started: 30 June 2026

The above studies echo critiques from the fields of geophysics and turbulence, where the sensitivity of scaling metrics to resolution, finite domain-size effects (truncation), and noise have long been recognized (Halley et al., 2004; Falconer, 1988). While such limitations have been acknowledged in the sea ice modeling community (e.g., Weiss 2001b; Bouillon and Rampal 2015b; Bouchat and Tremblay 2020), they have not been systematically addressed. In the application of scaling metrics to sea ice deformation, a further and largely overlooked source of complexity arises from the coarse-graining procedure itself. Although the diagnostic targets positive-definite strain rates, the coarse-graining is performed on signed velocity gradient components. As a result, positive and negative gradients (e.g., divergence and convergence, or opposing shear orientations) can partially cancel within coarse-graining boxes. Studies on signed measures have shown that such cancellation effects can influence apparent scaling independently of spatial organization in the underlying field (Ott et al., 1992; Bertozzi and Chhabra, 1994; Sorriso-Valvo et al., 2002). While it is recognized that scaling analysis of strain rates (scalar fields) ignores the directional or tensorial information of the field (Weiss and Marsan, 2004), the interaction between different modes of deformation, such as divergence, convergence, and positive/negative shear, remains unexplored in the sea ice literature.

In this study, we focus on spatial scaling and extend the conclusions to temporal scaling, as the two diagnostics rely on equivalent coarse-graining procedures. Our central question is: what mechanisms primarily control the scaling exponent? To address this, we construct synthetic deformation fields in controlled experiments where the underlying structure, sign, orientation, and noise characteristics are explicitly prescribed. This approach allows us to quantify the influence of each mechanism on first-order scaling. We then test these conclusions on deformation fields derived from high-resolution satellite observations (RGPS; Kwok et al., 1998) and on model outputs from the Sea Ice Rheology Experiment (SIREx; Bouchat et al., 2022a).

We find that coarse-graining introduces partial cancellation between positive and negative velocity gradients, which gives rise to scale-dependence in sea ice deformation. As a consequence, the scaling exponent is not strictly invariant under rotation, as physically equivalent strain fields can result in different scale-dependence when expressed in a different reference frame – a necessary condition for a statistically meaningful model evaluation diagnostic (Dukhovskoy et al., 2015). This highlights fundamental limitations in the use of scaling exponents as model evaluation metrics.

The paper is organized as follows. Section 2 introduces the data (synthetic, radarsat-derived observations and models), the scaling analysis method, and the experimental setup. Section 3 presents results from coarse-graining experiments applied to synthetic data and examines the implications for model evaluation. Conclusions are summarized in Section 4.

2 Data and Method

2.1 Data

We use deformation estimates from the RADARSAT Geophysical Processor System (RGPS) Lagrangian motion dataset (Bouchat and Hutter, 2022). We analyze the RGPS velocity gradient product, which provides deformation at a nominal spatial resolution of 10 km and a temporal resolution of three days. The sampling is inherently non-uniform because individual ice parcels are not always updated on the same dates, and some SAR image pairs cannot be tracked. Data are available for the

https://doi.org/10.5194/egusphere-2026-2911
Preprint. Discussion started: 30 June 2026

months of January to March from 1997 to 2008, corresponding to the period (winter) during which RGPS has been most widely used for deformation scaling studies (e.g. Bouchat et al. 2022b; Bouillon and Rampal 2015b; Hutter et al. 2018).

We also use simulated deformation estimates from the Sea Ice Rheology Experiment (SIREx) models (Bouchat et al., 2022a), covering a wide range of spatial resolutions (therefore LKF density and spatial localization) and model physics (EVP, VP, EAP, MEB). The velocity derivatives all have a temporal and spatial resolution of 3-days and 10-km (as the RGPS composite), regardless of the original resolution of the model output. The model's velocity gradient domains are masked according to the same 3-day data availability from the corresponding RGPS frames. More details about the models can be found in Bouchat et al. (2022b) and Hutter et al. (2022). We use data from the months of January to March 1997 and 2008, as available.

2.2 Spatio-Temporal Scaling

Power-law scaling of an observable $M(x)$ is defined mathematically as $M(\lambda x) = \lambda^{-\beta} M(x)$, where λ is a scaling factor, and β is a scaling exponent (Mandelbrot, 1977). In the case of scaling sea ice deformation, it describes how the domain averaged deformations $\langle \dot{\varepsilon}_{tot} \rangle_{L^n}$ change with scale L^n, where $L^n = 2^n \Delta x$ for $n = 0, 1, 2, ..., 10$, i.e.,

$$\frac{\langle \dot{\varepsilon}_{tot} \rangle_{L^{n+1}}}{\langle \dot{\varepsilon}_{tot} \rangle_{L^n}} \propto L^{-\beta}, \tag{1}$$

for all n.

Following Marsan et al. (2004) and current practice in the sea ice deformation community, we calculate the spatial mean total deformation at the native grid scale Δx = 10 km from the velocity derivatives over the full domain. At larger scales, a coarse-graining approach is used, where velocity gradients are averaged within boxes of increasing size $L^n \times L^n$ (see Figure 1). This corresponds to scales ranging from $L^0 = 1\Delta x$ (=10 km) to $L^{10} = 1024\Delta x$ (=10 240 km). Each subsequent box at the next larger scale L^{n+1} is centered on the grid node of the previous scale and overlaps adjacent boxes by $L^n/2$ to ensure sufficient statistical over sampling. To minimize biases, only boxes with at least 50% of non-masked grid cells are retained for analysis.

The divergence ($\dot{\varepsilon}_I$) and maximum shear strain rate ($\dot{\varepsilon}_{II}$) are defined as the first (trace) and second (determinant) invariants of the 2D sea ice deformation tensor ($\mathbf{L}$), which can be written as (ignoring the rotational component)

$$\mathbf{L} \approx \begin{bmatrix} \frac{\partial u}{\partial x} & \frac{1}{2}\left(\frac{\partial u}{\partial y} + \frac{\partial v}{\partial x}\right) \\ \frac{1}{2}\left(\frac{\partial u}{\partial y} + \frac{\partial v}{\partial x}\right) & \frac{\partial v}{\partial y} \end{bmatrix}, \tag{2}$$

where the diagonal terms are the axial strain rates and the off-diagonal terms are the shear strain rates. Finally, the first and second strain rate invariants and the total strain rates are calculated from the coarse-grained (averaged) velocity gradients as

$$\overline{\dot{\varepsilon}_I} = \overline{\frac{\partial u}{\partial x}} + \overline{\frac{\partial v}{\partial y}}, \tag{3}$$

https://doi.org/10.5194/egusphere-2026-2911
Preprint. Discussion started: 30 June 2026

$$\overline{\dot{\varepsilon}_{II}} = \left[\left(\overline{\frac{\partial u}{\partial x}} - \overline{\frac{\partial v}{\partial y}} \right)^2 + \left(\overline{\frac{\partial u}{\partial y}} + \overline{\frac{\partial v}{\partial x}} \right)^2 \right]^{1/2}, \tag{4}$$

$$\overline{\dot{\varepsilon}_{tot}} = \left[\overline{\dot{\varepsilon}_I}^2 + \overline{\dot{\varepsilon}_{II}}^2 \right]^{1/2}, \tag{5}$$

where $\overline{\dot{\varepsilon}_{tot}}$ is the weighted average of non-masked grid cells within each box (hereafter referred to as $\dot{\varepsilon}_{tot}$). This correction ensures consistent characterization of deformation across scales, regardless of data coverage. Note that if the field contains only one strain rate invariant (e.g., $\dot{\varepsilon}_I$), then $\overline{\dot{\varepsilon}_{tot}} = |\overline{\dot{\varepsilon}_I}|$. The scaling exponent β is calculated by fitting a power-law to the mean total deformation rate $\langle \dot{\varepsilon}_{tot} \rangle_L$ at each scale L in log-log space. Note that we use *scale dependence* to describe variations in $\langle \dot{\varepsilon}_{tot} \rangle_L$ with L. Theoretically, when this relationship is log-linear over at least two orders of magnitude, it is referred to as *scaling* and characterized by the scaling exponent β. Because this criterion is rarely strictly satisfied for sea ice strain rates, we refer to approximately log-linear relationships spanning more than one order of magnitude as scaling, following common practice in the field. Accordingly, the power-law fit of sea ice deformation is restricted to scales between 10 and 640 km (e.g., Marsan et al. 2004; Rampal et al. 2019; Bouchat et al. 2022b).

We retain the coarse-graining procedure introduced by Marsan et al. (2004) and do not apply the data-quality weighting proposed by Bouchat and Tremblay (2020). This weighting artificially enhances the influence of the distribution tails and produces β values substantially larger than those obtained from the original fields (Bouchat and Tremblay, 2020; Bouchat et al., 2022b). Using synthetic fields with added white noise (signal-to-noise ratio of 10), we find that noise does not significantly affect the scaling exponent (results not shown). The weighting procedure has a much larger impact on the estimated scaling than the noise itself.

2.3 Experimental setup

We prescribe idealized, user-defined strain rates to assess the behavior of standard first-order scaling diagnostics in idealized deformation fields. This approach allows independent variation of the strain-rate intensity, divergence–shear ratio, spatial localization, orientation, LKF spacing (s), and signal-to-noise ratio (SNR), making it possible to assess the influence of each factor separately. All experiments are performed on a square domain of dimensions 1024 × 1024 ($N_x \times N_x$) with 10-km (Δx) spatial resolution akin to the RADARSAT Geophysical Processor System (RGPS; Kwok et al. 1998) used in previous studies (e.g. Bouchat et al. 2022b; Stern and Lindsay 2009). For simplicity and without loss of generality, we consider deformations with velocities (u and v fields) that depend only on x or y.

The u and v fields are calculated by simple integration, assuming zero velocity at the wall , e.g., $u(x) = \int_0^x \frac{du}{dx} dx$. We use a C-grid with the vector quantities defined on the vertices of the grid cells and strain invariants defined at the grid centers (see Figure 2), as:

$$\frac{\partial u}{\partial x} = \frac{u_{i+1,j} - u_{i,j}}{\Delta x}, \tag{6}$$

https://doi.org/10.5194/egusphere-2026-2911
Preprint. Discussion started: 30 June 2026

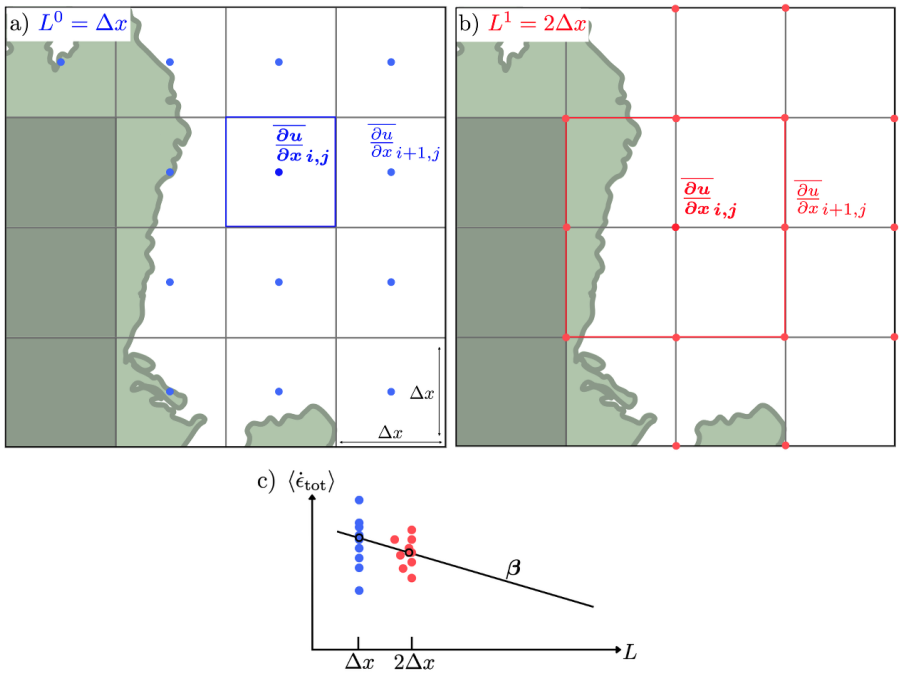

Figure 1. Schematic of the coarse-graining procedure and scaling analysis of one axial strain component only ($\partial u/\partial x$) on a domain (not to scale) with ocean (white) and land covered area (gray). Panels a and b show the velocity gradients, and mean velocity gradients over the first two scales (L^0, L^1) of size $L^0 = 2^0\Delta x = 10$km (blue) and $L^1 = 2^1\Delta x = 20$km (red), respectively. The analysis includes only ocean grid cells (white) and coarse-grained cells with >50% ocean coverage. Strain rates at different scales are derived from the averaged gradients at each scale (see Eqs. 3, 4, and 5). Panel c shows the mean total deformation $\langle \dot{\epsilon}_{\text{tot}} \rangle$ for the first two scales on a log-log plot for each box (full circles) and for the mean of all coarse-grained boxes (circles with black contour). The scaling exponent β is estimated using a least-squares linear fit in log-log space applied to the mean values. Note that the mean total deformation (colored circles) is calculated over a gradually smaller number of boxes $\left(= N_x^2 \text{ for n = 0, otherwise = } \left(\frac{N_x}{n} - 1\right)^2\right)$ with increasing scales $n = 0, 1, 2, ..., 10$.

$$\frac{\partial v}{\partial y} = \frac{v_{i,j+1} - v_{i,j}}{\Delta y}, \tag{7}$$

$$\frac{\partial u}{\partial y} = \frac{u_{i+1,j+1} + u_{i,j+1}}{2\Delta y} - \frac{u_{i+1,j-1} + u_{i,j-1}}{2\Delta y}, \tag{8}$$

$$\frac{\partial v}{\partial x} = \frac{v_{i+1,j+1} + v_{i+1,j}}{2\Delta x} - \frac{v_{i-1,j+1} + v_{i-1,j}}{2\Delta x}. \tag{9}$$

Note that off-diagonal terms of the deformation matrix $\left(\frac{\partial u}{\partial y} \text{ and } \frac{\partial v}{\partial x}\right)$ have a larger stencil than the diagonal terms and therefore introduce asymmetry in the $x-$ and $y-$directions.

https://doi.org/10.5194/egusphere-2026-2911
Preprint. Discussion started: 30 June 2026

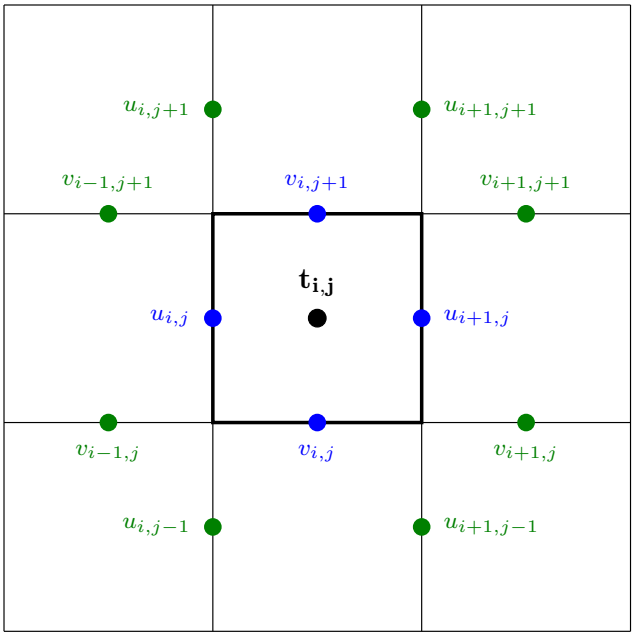

Figure 2. C-grid with scalars $\boldsymbol{t_{i,j}}$ ($\dot{\varepsilon}_I$, $\dot{\varepsilon}_{II}$, $\dot{\varepsilon}_{tot}$) defined at the center of the grid cell and vectors ($u_{i,j}$, $v_{i,j}$) defined on the vertical and horizontal vertices respectively. The stencils of the diagonal and off-diagonal terms in the deformation tensor are shown in blue and green respectively.

3 Results and Discussion

The synthetic fields consist of idealized LKFs represented as parallel bands of deformation. This simplified geometry provides a clean baseline for identifying which aspect of the deformation field determines the observed scale dependence. In the following, we use *spatial localization* to denote the spatial concentration of deformation. Conversely, low localization corresponds to a smoothly varying deformation field. Deformation intensity, in turn, refers to the magnitude of strain rates.

3.1 Spatial localization does not produce scale dependence

We first show that power-law scaling does not result from spatial localization using a domain where axial strain is localized along one-grid-cell-wide LKFs with regular spacing $s = k\Delta x$ for integer k forming a discrete set of delta-like discontinuities (Fig. 3). To this end, we calculate analytically the mean deformation at the smallest and largest scales and demonstrate that they are identical, implying $\beta = 0$. For a constant, positive-definite sea ice deformation ($\dot{\varepsilon}_0 = \sqrt{2}\partial u/\partial x > 0$, see Fig. 3a), the mean total deformation $\langle \dot{\varepsilon}_{tot} \rangle$ at the smallest scale can be written as

$$\langle \dot{\varepsilon}_{tot} \rangle_{L=\Delta x} = \frac{1}{N_x^2} \sum_{k=1}^{N_x^2/s} |\dot{\varepsilon}_0(ks)| = \frac{\dot{\varepsilon}_0}{s}. \tag{10}$$

https://doi.org/10.5194/egusphere-2026-2911
Preprint. Discussion started: 30 June 2026

Similarly, we write the mean total deformation at the largest scale

$$\langle \dot{\varepsilon}_{tot} \rangle_{L=N} = \left| \frac{1}{{N_x}^2} \sum_{k=1}^{{N_x}^2/s} \dot{\varepsilon}_0(ks) \right| = \frac{\dot{\varepsilon}_0}{s}. \tag{11}$$

Both are equal because the velocity gradients have the same sign everywhere. This is confirmed numerically for a range of different LKF amplitudes, orientations, spacing, domain size, and strain rates (i.e. shear or divergence; Fig. 3b). Spatial localization therefore does not result in scale dependence.

3.2 Signed velocity gradients produces scale dependence through cancellation

When introducing both positive and negative velocity gradients – as bands of alternating signs of divergence and/or shear strain rates ($\dot{\varepsilon}_I = (-1)^k \dot{\varepsilon}_0$ for integer k) – along the same LKFs (Fig. 3c), scale dependence emerges. At the smallest scale, the mean total deformation $\langle \dot{\varepsilon}_{tot} \rangle$ remains the same by definition ($\dot{\varepsilon}_0/s$) since we consider only the positive root in the mean total deformation rate (Eq. 5, for the positive-definite case), yet the mean large-scale total deformation is equal to zero because of cancellation between the positive and the negative strain rates

$$\langle \dot{\varepsilon}_{tot} \rangle_{L=N} = \left| \frac{1}{{N_x}^2} \sum_{k=1}^{{N_x}^2/s} \dot{\varepsilon}_0(ks) \right| = \left| \frac{1}{{N_x}^2} \sum_{k=1}^{{N_x}^2/s} (-1)^k \dot{\varepsilon}_0 \right| = 0. \tag{12}$$

The difference in mean total deformation between the smallest and largest scales implies scale-dependence at least between a range of scales (Fig 3d). Not surprisingly there is no scale dependence ($\beta = 0$) when the averaging box is smaller than the LKF spacing ($L < s$) where the deformation rates are unsigned or when the averaging box is much larger than the LKF spacing ($L >> s$) resulting in near total signed-gradient cancellation for all scales. Generally the scale-dependence is present over scales where $L > s$ and $L >> s$ except when $s = 2^n$. In this case, we see a discontinuity (break) in mean total deformation exactly at $L = s$. This behavior is robust to the exact choice of LKF spacing, PDF of intensity, or alignment with the coarse-graining boxes (results are not shown). These results establish signed-gradient cancellation as both necessary and sufficient for scale dependence. It also follows that – keeping the ratio of positive and negative velocity gradients constant – the scale-dependence is proportional to deformation intensity since $\langle \dot{\varepsilon}_{tot} \rangle_{\Delta x}$ increases while $\langle \dot{\varepsilon}_{tot} \rangle_N$ remains constant (see Fig. 6d). Implications from these mechanisms for model evaluation against observations are explored in Section 3.5.

3.3 Continuous deformation fields produce scale dependence through signed velocity gradient cancellation

We showed above that signed-gradient cancellation produces scale dependence as opposed to discontinuity or localization in the deformation field. Here, we repeat the same analysis with a continuous (non-localized) signed velocity gradient field (unsigned not shown) $u = \frac{\lambda}{2\pi} \dot{\varepsilon}_0 \cos\left(\frac{2\pi x}{\lambda}\right)$, where the wavelength λ (in grid cells) is a factor of the domain size N_x and is well resolved by the grid spacing Δx (Fig. 3d). In this case, the mean total deformation $\langle \dot{\varepsilon}_{\mathrm{tot}} \rangle$ at the smallest scale and at the largest

https://doi.org/10.5194/egusphere-2026-2911
Preprint. Discussion started: 30 June 2026

(domain) scale are

$$\langle \dot{\varepsilon}_{\mathrm{tot}} \rangle_{L=\Delta x} = \frac{\dot{\varepsilon}_0}{N_x} \int_0^{N_x} \left| \sin\left(\frac{2\pi x}{\lambda}\right) \right| dx = \frac{\dot{\varepsilon}_0}{N_x} \left| \frac{2N_x}{\lambda} \int_0^{\lambda/2} \sin\left(\frac{2\pi x}{\lambda}\right) dx \right| = \frac{2\dot{\varepsilon}_0 \lambda}{\lambda 2\pi} \cos\left(\frac{2\pi x}{\lambda}\right) \Big|_0^{\lambda/2} = \frac{2\dot{\varepsilon}_0}{\pi}, \tag{13}$$

$$\langle \dot{\varepsilon}_{\mathrm{tot}} \rangle_{L=N} = \frac{\dot{\varepsilon}_0}{N_x} \left| \int_0^{N_x} \sin\left(\frac{2\pi x}{\lambda}\right) dx \right| = -\frac{\dot{\varepsilon}_0}{N_x} \frac{\lambda}{2\pi} \cos\left(\frac{2\pi x}{\lambda}\right) \Big|_0^{N_x} = 0. \tag{14}$$

Again, scale dependence is present at least for a range of scales between Δx and L for a well resolved continuous deformation field, as $\langle \dot{\varepsilon}_{\mathrm{tot}} \rangle_{L=N} < \langle \dot{\varepsilon}_{\mathrm{tot}} \rangle_{L=\Delta x}$. In a similar manner to the cases where the deformation is localized, the scale-dependence (which establishes the scaling exponent β) depends on the wavelength of the sinusoid and on its alignment with the coarse-graining boxes (Figure 3f). These results demonstrate that spatial localization is not a necessary condition for producing scale-dependence, and therefore non-zero β values. Non-localized and smooth deformation fields can exhibit scaling akin to RGPS if they contain positive and negative signed velocity gradients. Together, Sections 3.1-.3 establish that signed-gradient cancellation is the mechanism generating β, and that this mechanism operates regardless of whether deformation is localized or smooth. Note that these experiments are based on synthetic LKFs with divergence only ($\dot{\varepsilon}_I$; $\dot{\varepsilon}_{II} = 0$); the same conclusions hold for experiments with shear deformation, as the signed-gradient cancellation mechanism remains unchanged.

3.4 Scaling is not invariant under rotation

A direct consequence of signed-gradient cancellation is that β depends on the choice of reference frame used to express the deformation. We demonstrate this with two deformation configurations that are physically equivalent, differing only by a rotation of the reference frame (Fig. 4a; Popov, 1990). For instance, the set of LKFs consisting of vertical bands of uniaxial strain rate field with alternating sign ($\partial u/\partial x = \pm\dot{\varepsilon_0}$ and $\partial v/\partial y = \partial u/\partial y = \partial v/\partial x = 0$, presented in Section 3.2) is equivalent to bands of isotropic strain rate ($\partial u/\partial x = \partial v/\partial y = \pm\dot{\varepsilon_0}$) with shear strain rate ($\partial u/\partial y = \partial v/\partial x = \pm\dot{\varepsilon_0}$) in a frame of reference rotated by $45°$. Yet, the scale-dependence is not the same for both configurations. The difference arises because coarse-graining interacts differently with the spatial arrangement of signed velocity gradients in each configuration. In the non-rotated case, coarse-graining windows are aligned with the LKF structure, preserving a consistent balance of positive and negative gradients across scales. A $45°$ rotation redistributes the same strain field relative to the grid, such that coarse-graining windows sample a different mixture of positive and negative velocity gradients at each scale, resulting in a different scaling (Fig. 4b).

The non-invariance under rotation could, in principle, have consequences for model evaluation since simulated and observed sea ice deformation are computed on different grids (e.g., tripolar, curvilinear, polar stereographic). The same LKF will have a different distribution of velocity gradient components, and therefore scaling in different models and observations. Whether this effect is apparent in scaling analysis performed even over just one single day but with a wide range of LKF orientations is unclear. For example, when we rotate velocity gradients in RGPS for one given 3-day snapshot by an angle $\theta \in [0°, 180°]$ prior to the computation of scaling exponents, the resulting scaling exponent shows only weak sensitivity (Fig. 5). Presumably, this

https://doi.org/10.5194/egusphere-2026-2911
Preprint. Discussion started: 30 June 2026

averaging will be even more apparent when scaling is calculated over several days. While this effect is minimal, it constitutes a methodological inconsistency with the requirement that validation metrics be rotation invariant (Dukhovskoy et al., 2015), particularly given that models tend to simulate LKFs that are aligned with the grid orientation (Lemieux et al., 2025).

3.5 Implications for model evaluation

The controlled experiments presented in Sections 3.1-3 established that signed-gradient cancellation ($\langle\dot{\varepsilon}_{tot}\rangle_{\Delta x} \neq \langle\dot{\varepsilon}_{tot}\rangle_N$) is a necessary and sufficient condition for scale-dependence and scaling ($\beta > 0$). It follows that differences in β in observations and models should be quantifiable from $\langle\dot{\varepsilon}_{tot}\rangle_{\Delta x}$ and $\langle\dot{\varepsilon}_{tot}\rangle_N$ alone (Fig. 6). Note that the mean total deformation at the largest scale ($\langle\dot{\varepsilon}_{tot}\rangle_N$) always departs from the linear scale dependence due to finite domain effects (e.g., Bouchat et al. 2022b; Rampal et al. 2019). Whether the mean total deformation at the largest scale is really smaller due to finite domain effects or not is discussed in Section 3.6.

To test this hypothesis, we use the same two-point approximation of β (used in Section 3.1) calculated from the mean total deformation at the smallest (Δx) and largest (N) scales (referred to as $\tilde{\beta}$ in the following; Fig. 6):

$$\tilde{\beta} = \frac{\log\langle\dot{\varepsilon}_{tot}\rangle_{\Delta x} - \log\langle\dot{\varepsilon}_{tot}\rangle_N}{\log\Delta x - \log N}, \tag{15}$$

where

$$\langle\dot{\varepsilon}_{tot}\rangle_{\Delta x} = \left\langle \left(\left(\frac{\partial u}{\partial x} + \frac{\partial v}{\partial y}\right)^2 + \left(\frac{\partial u}{\partial x} - \frac{\partial v}{\partial y}\right)^2 + \left(\frac{\partial u}{\partial y} + \frac{\partial v}{\partial x}\right)^2 \right)^{1/2} \right\rangle, \tag{16}$$

$$\langle\dot{\varepsilon}_{tot}\rangle_N = \left(\left(\overline{\frac{\partial u}{\partial x}} + \overline{\frac{\partial v}{\partial y}}\right)^2 + \left(\overline{\frac{\partial u}{\partial x}} - \overline{\frac{\partial v}{\partial y}}\right)^2 + \left(\overline{\frac{\partial u}{\partial y}} + \overline{\frac{\partial v}{\partial x}}\right)^2 \right)^{1/2}. \tag{17}$$

In contrast with β, which is estimated using all spatial scales, $\tilde{\beta}$ carries no "scale" information, and can be derived from the Probability Density Functions (PDFs) of the velocity gradients alone. The two-point approximation $\tilde{\beta}$ is strongly correlated with β (r = 0.92) across the 11 winters covered by RGPS observations and SIREx model configurations, covering all spatial resolutions and rheological configurations (Figure 7a). This relationship is also substantially stronger than that obtained with geometric LKF metrics (e.g., total length, density, growth rate) tested by Hutter et al. (2022). The departure from linearity of $\langle\dot{\varepsilon}_{tot}\rangle_N$ introduces a positive bias. This bias is comparable with both the sensitivity of β to the spatial-scale range used in its calculation and the observed or simulated inter-winter variability (Bouchat and Tremblay, 2020; Bouillon and Rampal, 2015b).

From the principle of variance addition (Casella and Berger, 2002),

$$\mathrm{Var}(\tilde{\beta}) = \frac{\mathrm{Var}(\log\langle\dot{\varepsilon}_{tot}\rangle_{\Delta x}) + \mathrm{Var}(\log\langle\dot{\varepsilon}_{tot}\rangle_N) - 2\mathrm{Cov}(\log\langle\dot{\varepsilon}_{tot}\rangle_{\Delta x}, \log\langle\dot{\varepsilon}_{tot}\rangle_N)}{(\log\Delta x - \log N)^2}, \tag{18}$$

we note that the large variance contributions associated with the deformation intensity (345%, $\langle\dot{\varepsilon}_{tot}\rangle_{\Delta x}$) and the deformation mean (161%, $\langle\dot{\varepsilon}_{tot}\rangle_N$) are compensated by their strong covariance (-406%), resulting in a comparatively small variance in $\tilde{\beta}$ (see cluster of points in Fig 7a and more diffuse cloud of points in Fig. 7bc). For example, FESOM has $\tilde{\beta}$ values similar to

https://doi.org/10.5194/egusphere-2026-2911
Preprint. Discussion started: 30 June 2026

those of other models, arising from an anomalously low deformation intensity ($\langle\dot{\varepsilon}_{tot}\rangle_{\Delta x}$) compensated by an anomalously small deformation mean ($\langle\dot{\varepsilon}_{tot}\rangle_N$). A consequence is that increasing model spatial resolution, i.e. increasing deformation intensity, has little impact on $\tilde{\beta}$ because it also increases the mean (Lemieux et al., 2025; Bouchat et al., 2022b; Spreen et al., 2017; Williams and Tremblay, 2018; Hutter et al., 2022). In contrast, the separation between the cloud of observed and simulated $\tilde{\beta}$ (and β; Fig. 7a) is due to the difference in magnitude of deformation $\langle\dot{\varepsilon}_{tot}\rangle_{\Delta x}$ (Fig. 7b), rather than the mean $\langle\dot{\varepsilon}_{tot}\rangle_N$ (Fig. 7c). This is consistent with RGPS gradient distributions having heavier tails than those of sea ice models (e.g., see MITgcm and FESOM in Fig. 8, left column).

To further examine the respective roles of deformation intensity and mean in controlling β in RGPS deformation fields, we perturbed the velocity gradient distributions (i) by multiplying all gradients by a factor γ, which modifies intensity while largely preserving the mean of the signed distribution, and (ii) by shifting all gradients by a constant δ, which modifies the deformation mean while leaving intensity approximately unchanged. In both cases, β responds predictably and monotonically to γ and δ, consistent with the analytical framework derived from synthetic fields (Fig. 9). This confirms that the mechanism identified in Sections 3.1–.3 (i) also operates in observed deformation fields, (ii) is not an artifact of the idealized geometry of the synthetic experiments, and (iii) modulates β without changing the spatial distribution of strain rates.

This two-point approximation framework offers an alternative interpretation of the seasonal cycle of β reported in Stern and Lindsay (2009), Hutter et al. (2018) and Lei et al. (2021). These studies attributed the higher summer (JJ) values of β, compared to those during winter (JFMA), to weaker ice and reduced stress transmission resulting in less long-range connectivity between floes. Here, we suggest these higher values may instead reflect increased deformation intensity. During summer, a looser ice pack is characterized by larger mean deformation rates despite weaker winds (Rampal et al., 2009), resulting in higher β even without increased localization. In winter, deformation is more localized, but the magnitude of velocity gradients across leads is smaller, resulting in less deformation intensity (smaller $\langle\dot{\varepsilon}_{tot}\rangle_{\Delta x}$) and lower β. These interpretations are not contradictory; they emphasize that the link between localization and scaling is indirect and mediated by deformation statistics. The role of mean deformation ($\langle\dot{\varepsilon}_{tot}\rangle_N$) in seasonal variability, on the other hand, remains less well constrained. For instance, fall and early-winter conditions, when the pack is not yet consolidated, can accommodate net convergence (Richter-Menge and Farrell, 2013), which reduces signed-gradient cancellation (larger $\langle\dot{\varepsilon}_{tot}\rangle_N$) and may be partially offset by increases in deformation magnitude. Quantifying the seasonal and spatial variability of the deformation intensity and mean is left for future work.

3.6 Break of scaling at large scale

In Section 3.2, we showed that lower mean total deformation and break in scaling emerge from the characteristic spacing of opposing-sign gradient regions rather than from domain truncation. This suggests that the break in RGPS scaling at the largest scale (640 km or $2^6\Delta x$) – previously attributed to finite-size effects on the grounds that the coarse-graining domain becomes too large relative to deformation structures (e.g., Bouchat and Tremblay, 2020; Ouillon et al., 1996) – may instead reflect a characteristic physical scale of the deformation field itself, namely the dominant spacing between large regions of opposing-sign velocity gradients. To test this hypothesis, we progressively reduced the RGPS domain by a factor of 2 and 4, with respect to the domain centroid. If the break in mean total deformation were a finite-size artifact, we should observe a shift in break

https://doi.org/10.5194/egusphere-2026-2911
Preprint. Discussion started: 30 June 2026

toward smaller scales as the domain shrinks. Figure 10 confirms that it does not; the scaling breaks at 640 km independently of the domain size. This result is robust to the exact choice of the day analyzed (result not shown). The practical implication is that routinely truncating the scaling window at 640 km and treating the departure as an artifact is not justified. The drop-off carries physical information about the basin-scale organization of opposing-sign deformation, which could be linked to synoptic scales or coastline geometry (Hutchings et al., 2005). Note that our domain reduction experiment is performed independently of LKF positions and therefore may not resample the field in a statistically controlled way. A detailed analysis is beyond the scope of this study.

3.7 Power Spectra

Another avenue for characterizing localization in sea ice deformation from kinematics is to look at the spectrum in wavenumber space of the mean total strain rates (see for example Jendersie et al. 2025). Results show a nearly constant radially averaged power spectral density (RAPSD) slope, in both RGPS and models (blue curves; Fig. 11) – except those that produce very diffuse deformation fields and do not resolve localized deformation features such as LKFs (pink curves, Fig. 11; see also Bouchat et al. 2022b for spatial maps of deformation fields). Sharp velocity gradients associated with LKFs (i.e., discontinuities in the velocity field) require contributions from many wavenumbers to be reconstructed, starting from those associated with the synoptic-scale spacing between dominant LKFs. Consequently, spectral slopes provide limited ability to discriminate between sea ice models once they can produce localized LKFs, even if the LKF density is low. Note that this result differs from Kolmogorov turbulence, where spectral slopes reflect an energy cascade from larger to smaller scales and thus encode information about the underlying dynamics.

Note that these results come with important caveats. First, spectral analysis measures the distribution of variance across wavenumbers and is therefore insensitive to intermittency: fields with identical spectra can differ strongly in higher-order statistics and extreme events, which are captured by structure functions but not by spectra (Turcotte, 1997). Spectra therefore do not provide access to multifractal scaling, which requires moment-dependent statistics. Second, spectral estimation assumes stationarity and isotropy, neither of which is strictly satisfied for sea ice deformation. Together, these limitations mean that spectral slopes characterize only part of the spatial variability and cannot fully constrain the organization of intermittent, anisotropic deformation fields.

4 Conclusions

We use synthetic sea ice velocity gradient fields to isolate the mechanisms controlling the scale dependence of sea ice deformation. Results show that the scaling arises from coarse-graining–induced cancellation of signed velocity gradients – characterized by the intensity and the mean (e.g., ratio of opening and closing) of sea ice deformation – rather than from the spatial localization of deformation. The scaling reflects the cancellation of signed-gradients at various scales, rather than scale dependence of the deformation itself. The scaling exponent β is strongly influenced by the statistical properties of the velocity gradient

https://doi.org/10.5194/egusphere-2026-2911
Preprint. Discussion started: 30 June 2026

probability distribution (PDF), i.e., is implicitly a coarse summary of these distributions, reflecting the balance between their intensity and their mean.

As a consequence, sea ice deformation PDFs with different widths and means can yield similar values of β, which fundamentally limits its discriminative power as a diagnostic of sea ice rheology. For instance, diffuse, weakly localized deformation can have scaling exponents comparable to those of a highly localized, fracture-dominated ice pack, as the mean divergence is near zero. Similarly, an active sea ice cover dominated by shear events may result in β values comparable to those of a weakly deforming system with balanced opening and closing rates. These regimes are dynamically distinct, yet remain indistinguishable from scaling alone.

For model evaluation, this points toward diagnostics that target gradient distributions directly. PDF-based comparisons of velocity gradients and strain invariants – e.g., evaluated bin-wise as suggested in Bouchat et al. (2022b) – provide a more physically interpretable assessment of model performance than β alone. Importantly, PDF-based approaches do not require fully gridded strain-rate fields, enabling the use of emerging satellite products, including high-resolution velocity gradients from Sentinel-1 and the RADARSAT Constellation Mission, to study the spatial and temporal variation in sea ice statistics (Plante et al., 2025). Geometric diagnostics such as LKF density, length, and intersection angle distribution (Hutter and Losch, 2020; Hutter et al., 2022; Ringeisen et al., 2023), and even power spectra, capture geometric information, including localization, that β does not reflect. In the absence of complementary diagnostics, the scaling exponent alone provides limited and potentially ambiguous constraints on model rheology.

Methodologically, the scale dependence is not invariant under a rotation of the reference frame. Two physically equivalent deformation fields can result in different scale dependence. While the practical effect is modest for RGPS fields with diverse LKF orientations, it constitutes a methodological inconsistency. Moreover, the break in scaling at ~ 640 km is independent of domain size, suggesting it reflects a physical characteristic scale of the deformation field rather than finite-size effects, such as spatial heterogeneity in deformation (e.g., coexistence of highly active regions and quiescent areas or of highly convergent and divergent areas).

More generally, this study highlights a limitation of current sea ice deformation metrics, an issue also raised in SIREx (Bouchat et al., 2022b; Hutter et al., 2022). There is a lack of diagnostics capable of disentangling the statistical properties of deformation from the scale invariance of strain rates within a unified framework. The existence and robustness of distinct scaling regimes across spatial scales and ice regimes (universality) – from ocean-driven variability at small scales to internally driven stress transmission at larger scales – remain open questions (Weiss, 2001a; Lynmcnutt and Overland, 2003; Uusinoka et al., 2025b, a; Hutchings et al., 2011, 2024). These questions need to be addressed by developing targeted scale invariance diagnostics that are sensitive to non-stationarity, isotropy, and directional/tensorial information of the deformation fields, and by exploiting new high-resolution satellite datasets, which provide expanded spatial and temporal coverage in a changing Arctic sea ice system.

https://doi.org/10.5194/egusphere-2026-2911
Preprint. Discussion started: 30 June 2026

Code and data availability. All published data products can be found on Zenodo. This includes the ice velocity gradients from model outputs (https://zenodo.org/records/6321323; Bouchat et al. 2022a) and from RGPS (https://zenodo.org/records/6321327; Bouchat and Hutter 2022). All analysis codes are available on GitHub at https://github.com/flobeaudry/SISA.

Author contributions. FB and BT designed the experiments, and FB carried them out; FB developed the synthetic experiments and statistical analysis code; FB wrote the manuscript draft with contributions and reviews from BT.

Competing interests. Neither of the authors has any competing interests.

Acknowledgements. This work is a contribution to a Canadian Space Agency (CSA) Research Opportunity in Space Science (ROSS-Cycle III). Florence Beaudry is grateful for the scientific and financial support of McGill University and Québec-Océan. Bruno Tremblay is grateful for the financial support by the Natural Sciences and Engineering and Research Council (NSERC) Discovery Program and by Environment and Climate Change Canada (ECCC) via the Grants and Contributions program. The authors also thank Jean-François Lemieux, Mathieu Plante, Alexander Komarov, Damien Ringeisen and Félix St-Denis for their useful comments on this work.

https://doi.org/10.5194/egusphere-2026-2911
Preprint. Discussion started: 30 June 2026

References

Bertozzi, A. L. and Chhabra, A. B.: Cancellation exponents and fractal scaling, Physical Review E, 49, 4716–4719, https://doi.org/10.1103/PhysRevE.49.4716, 1994.

Bouchat, A. and Hutter, N.: Deformation composite of the RADARSAT Geophysical Processor System (RGPS) Lagrangian motion data, https://doi.org/10.5281/zenodo.6321327, 2022.

Bouchat, A. and Tremblay, B.: Using sea-ice deformation fields to constrain the mechanical strength parameters of geophysical sea ice, Journal of Geophysical Research: Oceans, 122, 5802–5825, https://doi.org/10.1002/2017JC013020, 2017.

Bouchat, A. and Tremblay, B.: Reassessing the Quality of Sea-Ice Deformation Estimates Derived From the RADARSAT Geophysical Processor System and Its Impact on the Spatiotemporal Scaling Statistics, Journal of Geophysical Research: Oceans, 125, e2019JC015 944, https://doi.org/10.1029/2019JC015944, 2020.

Bouchat, A., Hutter, N., Chanut, J., Dupont, F., Dukhovskoy, D., Garric, G., Lee, Y., Lemieux, J.-F., Lique, C., Losch, M., Maslowski, W., Myers, P. G., Ólason, E., Rampal, P., Rasmussen, T., Talandier, C., Tremblay, B., and Wang, Q.: Model Lagrangian trajectories and deformation data analyzed in the Sea Ice Rheology Experiment - Part I, https://doi.org/10.5281/zenodo.6321323, 2022a.

Bouchat, A., Hutter, N., Chanut, J., Dupont, F., Dukhovskoy, D., Garric, G., Lee, Y. J., Lemieux, J.-F., Lique, C., Losch, M., Maslowski, W., Myers, P. G., Ólason, E., Rampal, P., Rasmussen, T., Talandier, C., Tremblay, B., and Wang, Q.: Sea Ice Rheology Experiment (SIREx): 1. Scaling and Statistical Properties of Sea-Ice Deformation Fields, Journal of Geophysical Research: Oceans, 127, e2021JC017 667, https://doi.org/10.1029/2021JC017667, 2022b.

Bouillon, S. and Rampal, P.: Presentation of the dynamical core of neXtSIM, a new sea ice model, Ocean Modelling, 91, 23–37, https://doi.org/10.1016/j.ocemod.2015.04.005, 2015a.

Bouillon, S. and Rampal, P.: On producing sea ice deformation data sets from SAR-derived sea ice motion, The Cryosphere, 9, 663–673, https://doi.org/10.5194/tc-9-663-2015, 2015b.

Bourgault, P., Straub, D., Duquette, K., Nadeau, L.-P., and Tremblay, B.: Vertical Heat Fluxes beneath Idealized Sea Ice Leads in Large-Eddy Simulations: Comparison with Observations from the SHEBA Experiment, Journal of Physical Oceanography, 50, 2189–2202, https://doi.org/10.1175/JPO-D-19-0298.1, 2020.

Casella, G. and Berger, R. L.: Statistical inference, Brooks/Cole Cengage Learning, Australia, 2nd ed edn., ISBN 978-0-495-39187-6 978-0-534-24312-8 0-495-39187-5 0-534-24312-6, section: xxviii, 660 pages : illustrations ; 25 cm, 2002.

Coon, M. D., Knoke, G. S., Echert, D. C., and Pritchard, R. S.: The architecture of an anisotropic elastic-plastic sea ice mechanics constitutive law, Journal of Geophysical Research, 103, 21,915–21,925, https://doi.org/10.1029/98JC01259, 1998.

Dansereau, V., Weiss, J., Saramito, P., and Lattes, P.: A Maxwell elasto-brittle rheology for sea ice modelling, The Cryosphere, 10, 1339–1359, https://doi.org/10.5194/tc-10-1339-2016, 2016.

Dukhovskoy, D. S., Ubnoske, J., Blanchard-Wrigglesworth, E., Hiester, H. R., and Proshutinsky, A.: Skill metrics for evaluation and comparison of sea ice models, Journal of Geophysical Research: Oceans, 120, 5910–5931, https://doi.org/10.1002/2015JC010989, 2015.

Falconer, K.: Fractal Geometry: Mathematical Foundations and Applications, John Wiley & Sons, ISBN 978-1-118-76286-8, google-Books-ID: XJN7AgAAQBAJ, 1988.

Feder, J.: Fractals, Springer US, Boston, MA, ISBN 978-1-4899-2126-0 978-1-4899-2124-6, https://doi.org/10.1007/978-1-4899-2124-6, 1988.

https://doi.org/10.5194/egusphere-2026-2911
Preprint. Discussion started: 30 June 2026

Girard, L., Weiss, J., Molines, J. M., Barnier, B., and Bouillon, S.: Evaluation of high-resolution sea ice models on the basis of statistical and scaling properties of Arctic sea ice drift and deformation, Journal of Geophysical Research (Oceans), 114, C08 015, https://doi.org/10.1029/2008JC005182, 2009.

Halley, J. M., Hartley, S., Kallimanis, A. S., Kunin, W. E., Lennon, J. J., and Sgardelis, S. P.: Uses and abuses of fractal methodology in ecology, Ecology Letters, 7, 254–271, https://doi.org/10.1111/j.1461-0248.2004.00568.x, 2004.

Hamburger, D., Biham, O., and Avnir, D.: Apparent fractality emerging from models of random distributions, Physical Review E, 53, 3342–3358, https://doi.org/10.1103/PhysRevE.53.3342, 1996.

Hibler, W.: Dynamic Thermodynamic Sea Ice Model, Journal of Physical Oceanography, 9, 815–846, https://doi.org/10.1175/1520-0485(1979)009<0815:ADTSIM>2.0.CO;2, num Pages: 32 Place: Boston Web of Science ID: WOS:A1979HH81600014, 1979.

Hutchings, J. K., Heil, P., and Hibler, W. D.: Modeling Linear Kinematic Features in Sea Ice, Monthly Weather Review, 133, 3481–3497, https://doi.org/10.1175/MWR3045.1, 2005.

Hutchings, J. K., Roberts, A., Geiger, C. A., and Richter-Menge, J.: Spatial and temporal characterization of sea-ice deformation, Annals of Glaciology, 52, 360–368, https://doi.org/10.3189/172756411795931769, 2011.

Hutchings, J. K., Bliss, A. C., Mondal, D., and Elosegui, P.: Sea Ice Deformation Is Not Scale Invariant Over Length Scales Greater Than a Kilometer, Geophysical Research Letters, 51, e2024GL108 582, https://doi.org/10.1029/2024GL108582, 2024.

Hutter, N. and Losch, M.: Feature-based comparison of sea ice deformation in lead-permitting sea ice simulations, The Cryosphere, 14, 93–113, https://doi.org/10.5194/tc-14-93-2020, 2020.

Hutter, N., Losch, M., and Menemenlis, D.: Scaling Properties of Arctic Sea Ice Deformation in a High-Resolution Viscous-Plastic Sea Ice Model and in Satellite Observations, Journal of Geophysical Research: Oceans, 123, 672–687, https://doi.org/10.1002/2017JC013119, 2018.

Hutter, N., Bouchat, A., Dupont, F., Dukhovskoy, D., Koldunov, N., Lee, Y. J., Lemieux, J.-F., Lique, C., Losch, M., Maslowski, W., Myers, P. G., Ólason, E., Rampal, P., Rasmussen, T., Talandier, C., Tremblay, B., and Wang, Q.: Sea Ice Rheology Experiment (SIREx): 2. Evaluating Linear Kinematic Features in High-Resolution Sea Ice Simulations, Journal of Geophysical Research: Oceans, 127, e2021JC017 666, https://doi.org/10.1029/2021JC017666, 2022.

Ip, C. F., Iii, W. D. H., and Flato, G. M.: On the effect of rheology on seasonal sea-ice simulations, Annals of Glaciology, 15, 17–25, https://doi.org/10.3189/1991AoG15-1-17-25, 1991.

Jendersie, R., Lessig, C., and Richter, T.: A GPU parallelization of the neXtSIM-DG dynamical core (v0.3.1), Geoscientific Model Development, 18, 3017–3040, https://doi.org/10.5194/gmd-18-3017-2025, 2025.

Kreyscher, M., Harder, M., Lemke, P., and Flato, G. M.: Results of the Sea Ice Model Intercomparison Project: Evaluation of sea ice rheology schemes for use in climate simulations, Journal of Geophysical Research: Oceans, 105, 11 299–11 320, https://doi.org/10.1029/1999JC000016, 2000.

Kwok: Deformation of the Arctic Ocean Sea Ice Cover between November 1996 and April 1997: A Qualitative Survey, in: IUTAM Symposium on Scaling Laws in Ice Mechanics and Ice Dynamics, edited by Dempsey, J. P. and Shen, H. H., pp. 315–322, Springer Netherlands, Dordrecht, ISBN 978-94-015-9735-7, https://doi.org/10.1007/978-94-015-9735-7_26, 2001.

Kwok, R., Schweiger, A., Rothrock, D. A., Pang, S., and Kottmeier, C.: Sea ice motion from satellite passive microwave imagery assessed with ERS SAR and buoy motions, Journal of Geophysical Research: Oceans, 103, 8191–8214, https://doi.org/10.1029/97JC03334, 1998.

https://doi.org/10.5194/egusphere-2026-2911
Preprint. Discussion started: 30 June 2026

Lei, R., Hoppmann, M., Cheng, B., Zuo, G., Gui, D., Cai, Q., Belter, H. J., and Yang, W.: Seasonal changes in sea ice kinematics and deformation in the Pacific sector of the Arctic Ocean in 2018/19, The Cryosphere, 15, 1321–1341, https://doi.org/10.5194/tc-15-1321-2021, 2021.

Lemieux, J.-F., Plante, M., Hutter, N., Ringeisen, D., Tremblay, B., Roy, F., and Blain, P.: Impact of non-normal flow rule on linear kinematic features in pan-Arctic ice-ocean simulations, EGUsphere, pp. 1–33, https://doi.org/10.5194/egusphere-2024-3831, 2025.

Lynmcnutt, S. and Overland, J.: Spatial hierarchy in Arctic sea ice dynamics, Tellus, 55, https://doi.org/10.3402/tellusa.v55i2.12088, 2003.

Mandelbrot, B. B.: Fractals : form, chance, and dimension, San Francisco : W. H. Freeman, ISBN 978-0-7167-0473-7, http://archive.org/details/fractalsformchan0000mand, 1977.

Mandelbrot, B. B.: Self-Affine Fractals and Fractal Dimension, Physica Scripta, 32, 257, https://doi.org/10.1088/0031-8949/32/4/001, 1985.

Mandelbrot, B. B. and Wheeler, J. A.: The Fractal Geometry of Nature, American Journal of Physics, 51, 286–287, https://doi.org/10.1119/1.13295, 1983.

Marsan, D. and Weiss, J.: Space/time coupling in brittle deformation at geophysical scales, Earth and Planetary Science Letters, 296, 353–359, https://doi.org/10.1016/j.epsl.2010.05.019, 2010.

Marsan, D., Stern, H., Lindsay, R., and Weiss, J.: Scale Dependence and Localization of the Deformation of Arctic Sea Ice, Physical Review Letters, 93, 178 501, https://doi.org/10.1103/PhysRevLett.93.178501, 2004.

Martin, S. and Thorndike, A. S.: Dispersion of sea ice in the Bering Sea, Journal of Geophysical Research: Oceans, 90, 7223–7226, https://doi.org/10.1029/JC090iC04p07223, 1985.

McPhee, M. G., Kwok, R., Robins, R., and Coon, M.: Upwelling of Arctic pycnocline associated with shear motion of sea ice, Geophysical Research Letters, 32, https://doi.org/10.1029/2004GL021819, 2005.

Notz, D., Jahn, A., Holland, M., Hunke, E., Massonnet, F., Stroeve, J., Tremblay, B., and Vancoppenolle, M.: The CMIP6 Sea-Ice Model Intercomparison Project (SIMIP): understanding sea ice through climate-model simulations, Geoscientific Model Development, 9, 3427–3446, https://doi.org/10.5194/gmd-9-3427-2016, 2016.

Oikkonen, A., Haapala, J., Lensu, M., Karvonen, J., and Itkin, P.: Small-scale sea ice deformation during N-ICE2015: From compact pack ice to marginal ice zone, Journal of Geophysical Research: Oceans, 122, 5105–5120, https://doi.org/10.1002/2016JC012387, 2017.

Ott, E., Du, Y., Sreenivasan, K. R., Juneja, A., and Suri, A. K.: Sign-singular measures: Fast magnetic dynamos, and high-Reynolds-number fluid turbulence, Physical Review Letters, 69, 2654–2657, https://doi.org/10.1103/PhysRevLett.69.2654, 1992.

Ouillon, G., Castaing, C., and Sornette, D.: Hierarchical geometry of faulting, Journal of Geophysical Research: Solid Earth, 101, 5477–5487, https://doi.org/10.1029/95JB02242, 1996.

Plante, M., Lemieux, J.-F., Tremblay, L. B., Bouchat, A., Ringeisen, D., Blain, P., Howell, S., Brady, M., Komarov, A. S., Duval, B., Yakuden, L., and Labelle, F.: A sea ice deformation and rotation rate dataset (2017–2023) from the Environment and Climate Change Canada automated sea ice tracking system (ECCC-ASITS), Earth System Science Data, 17, 423–434, https://doi.org/10.5194/essd-17-423-2025, 2025.

Popov, E. P. E. P.: Engineering mechanics of solids, Prentice-Hall international series in civil engineering and engineering mechanics, Prentice Hall, https://cir.nii.ac.jp/crid/1970586434849213608, 1990.

Rampal, P., Weiss, J., Marsan, D., Lindsay, R., and Stern, H.: Scaling properties of sea ice deformation from buoy dispersion analysis, Journal of Geophysical Research: Oceans, 113, https://doi.org/10.1029/2007JC004143, 2008.

Rampal, P., Weiss, J., and Marsan, D.: Positive trend in the mean speed and deformation rate of Arctic sea ice, 1979–2007, Journal of Geophysical Research: Oceans, 114, https://doi.org/10.1029/2008JC005066, 2009.

https://doi.org/10.5194/egusphere-2026-2911
Preprint. Discussion started: 30 June 2026

Rampal, P., Dansereau, V., Olason, E., Bouillon, S., Williams, T., Korosov, A., and Samaké, A.: On the multi-fractal scaling properties of sea ice deformation, The Cryosphere, 13, 2457–2474, https://doi.org/10.5194/tc-13-2457-2019, 2019.

Richter-Menge, J. A. and Farrell, S. L.: Arctic sea ice conditions in spring 2009–2013 prior to melt, Geophysical Research Letters, 40, 5888–5893, https://doi.org/10.1002/2013GL058011, 2013.

Ringeisen, D., Hutter, N., and von Albedyll, L.: Deformation lines in Arctic sea ice: intersection angle distribution and mechanical properties, The Cryosphere, 17, 4047–4061, https://doi.org/10.5194/tc-17-4047-2023, 2023.

Rothrock, D. A. and Thorndike, A. S.: Measuring the sea ice floe size distribution, Journal of Geophysical Research: Oceans, 89, 6477–6486, https://doi.org/10.1029/JC089iC04p06477, 1984.

Savard, A. and Tremblay, B.: On the sensitivity of sea ice deformation statistics to plastic damage, The Cryosphere, 18, 2017–2034, https://doi.org/10.5194/tc-18-2017-2024, 2024.

Shy, T. L., Walsh, J. E., Chapman, W. L., Lynch, A. H., and Bailey, D. A.: Sea-ice model validation using submarine measurements of ice draft, Annals of Glaciology, 31, 307–312, https://doi.org/10.3189/172756400781820110, 2000.

Sorriso-Valvo, L., Carbone, V., Noullez, A., Politano, H., Pouquet, A., and Veltri, P.: Analysis of cancellation in two-dimensional magneto-hydrodynamic turbulence, Physics of Plasmas, 9, 89–95, https://doi.org/10.1063/1.1420738, 2002.

Spreen, G., Kwok, R., Menemenlis, D., and Nguyen, A. T.: Sea-ice deformation in a coupled ocean–sea-ice model and in satellite remote sensing data, The Cryosphere, 11, 1553–1573, https://doi.org/10.5194/tc-11-1553-2017, 2017.

Stern, H. L. and Lindsay, R. W.: Spatial scaling of Arctic sea ice deformation, Journal of Geophysical Research: Oceans, 114, https://doi.org/10.1029/2009JC005380, 2009.

Stern, H. L., Rothrock, D. A., and Kwok, R.: Open water production in Arctic sea ice: Satellite measurements and model parameterizations, Journal of Geophysical Research: Oceans, 100, 20 601–20 612, https://doi.org/10.1029/95JC02306, 1995.

Tian, T., Davy, R., Ponsoni, L., and Yang, S.: Impact of modulating surface heat flux through sea ice leads on Arctic sea ice in EC-Earth3 in different climates, The Cryosphere, 19, 2751–2768, https://doi.org/10.5194/tc-19-2751-2025, 2025.

Turcotte, D. L.: Fractals and Chaos in Geology and Geophysics, Cambridge University Press, Cambridge, 2 edn., ISBN 978-0-521-56733-6, https://doi.org/10.1017/CBO9781139174695, 1997.

Ungermann, M., Tremblay, L. B., Martin, T., and Losch, M.: Impact of the ice strength formulation on the performance of a sea ice thickness distribution model in the Arctic, Journal of Geophysical Research: Oceans, 122, 2090–2107, https://doi.org/10.1002/2016JC012128, 2017.

Uusinoka, M., Haapala, J., Åström, J., Lensu, M., and Polojärvi, A.: Scale invariance in kilometer-scale sea ice deformation, EGUsphere, pp. 1–17, https://doi.org/10.5194/egusphere-2025-311, 2025a.

Uusinoka, M., Savard, A., Åström, J., Haapala, J., and Polojärvi, A.: Threshold Domain Sizes for Multifractality in Sea Ice Deformation, Geophysical Research Letters, 52, e2025GL116 833, https://doi.org/10.1029/2025GL116833, 2025b.

Weiss, J.: Fracture and fragmentation of ice: a fractal analysis of scale invariance, Engineering Fracture Mechanics, 68, 1975–2012, https://doi.org/10.1016/S0013-7944(01)00034-0, 2001a.

Weiss, J.: Self-affinity of fracture surfaces and implications on a possible size effect on fracture energy, International Journal of Fracture, 109, 365–381, https://doi.org/10.1023/A:1011078531887, 2001b.

Weiss, J. and Marsan, D.: Scale properties of sea ice deformation and fracturing, Comptes Rendus Physique, 5, 735–751, https://doi.org/10.1016/j.crhy.2004.09.005, 2004.

Williams, J. and Tremblay, L. B.: The dependence of energy dissipation on spatial resolution in a viscous-plastic sea-ice model, Ocean Modelling, 130, 40–47, https://doi.org/10.1016/j.ocemod.2018.08.001, 2018.

https://doi.org/10.5194/egusphere-2026-2911
Preprint. Discussion started: 30 June 2026

Zhang, J. and Rothrock, D. A.: Effect of sea ice rheology in numerical investigations of climate, Journal of Geophysical Research: Oceans, 110, https://doi.org/10.1029/2004JC002599, 2005.

https://doi.org/10.5194/egusphere-2026-2911
Preprint. Discussion started: 30 June 2026

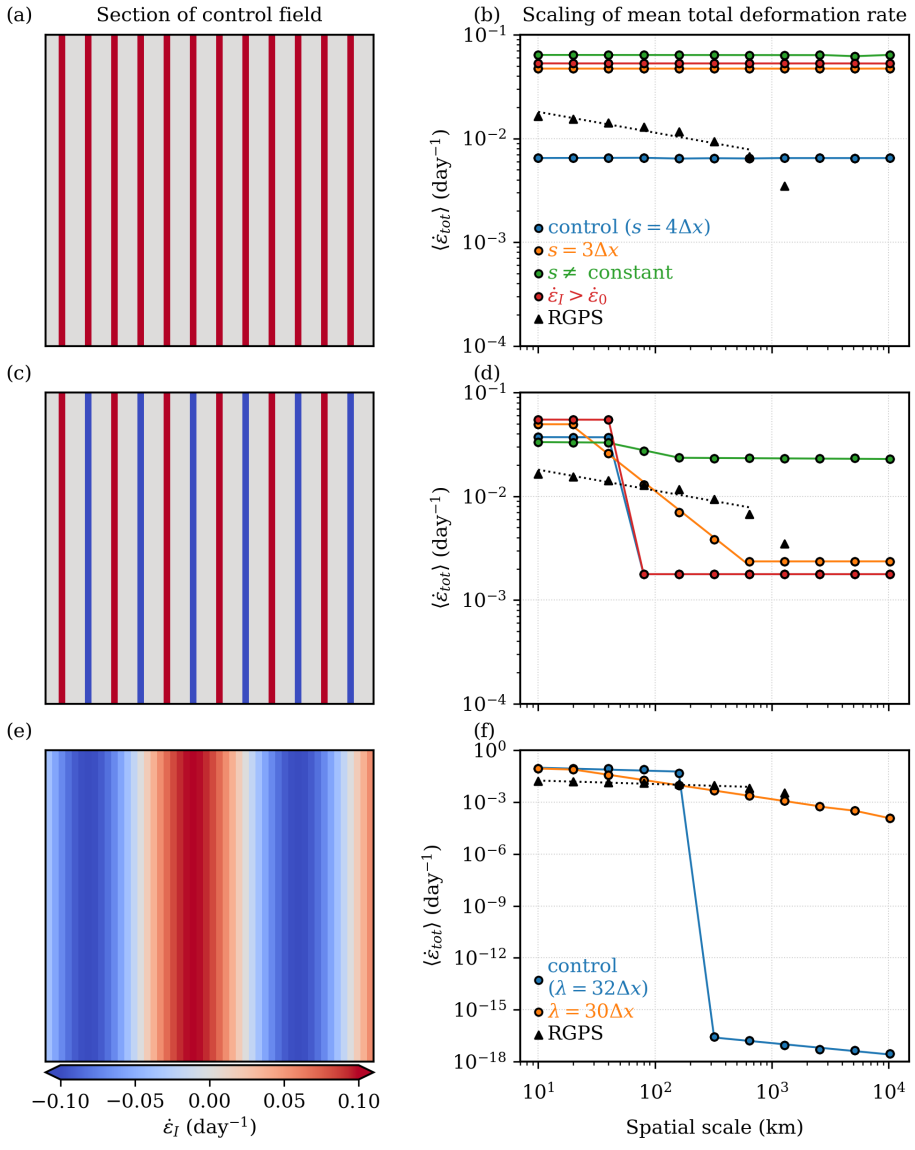

Figure 3. (a-c-e) Divergence fields for the three control cases. Field are shown over a subset of the domain for clarity. Localized positive-definite (a) and signed (c) divergence with spacing $s = 4\Delta x$, and (e) continuous (non-localized) sinusoidal divergence with wavelength $\lambda = 32\Delta x$. (b-d-f) Spatial scaling showing the mean total deformation as a function of spatial scale for the control case (blue), a spacing/wavelength that is not a factor of L ($s = 3\Delta x$ and $\lambda = 30\Delta x$; orange), irregular spacing (green), increased velocity gradient magnitude (red), and for the RGPS deformation on 29-31 January 2002 (black triangles). Localized positive-definite fields exhibit no scale-dependence (flat curves), whereas both localized signed and sinusoidal signed fields display scale-dependent behavior due to cancellation of signed velocity gradients during coarse-graining. The distribution of velocity gradients of cases displayed in panels c-f have a slight positive shift to allow for non-zero largest scale mean total deformation rate, and thus log-log plotting. The same results are obtained with pure shear or shear and divergence. Note that in panel d, the blue and red curves largely overlap, except at small scales.

https://doi.org/10.5194/egusphere-2026-2911
Preprint. Discussion started: 30 June 2026

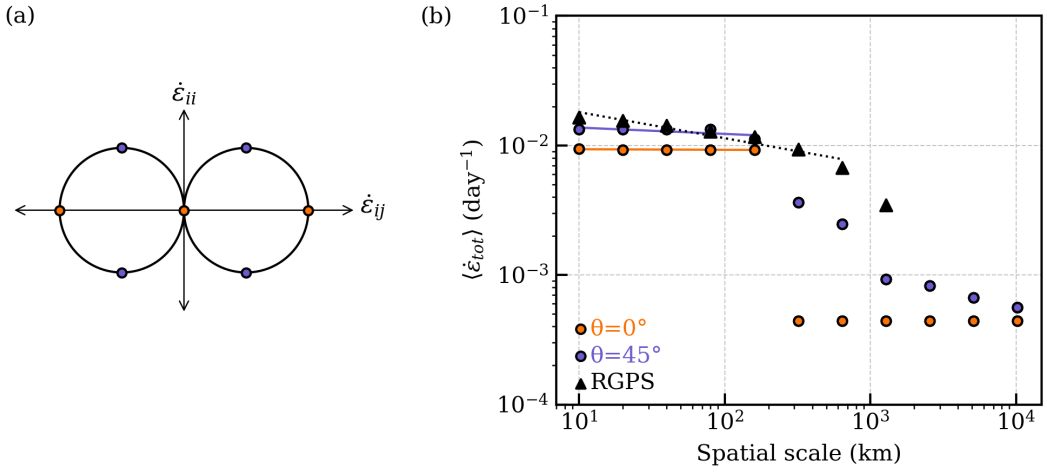

Figure 4. (a) Axial strain rate field for two identical deformation fields differing only by their frame of reference. (b) Scaling of mean total deformations as a function of spatial scale $L^n = 2^n \Delta x$ ($n = 0, 1, ..., 10$, Δx =10 km) for the two synthetic experiments with 0° (orange circles) and 45° (purple circles) rotation, both with regular spacing $s = 16\Delta x$ and for RGPS 29-31 January 2002 (black triangles).

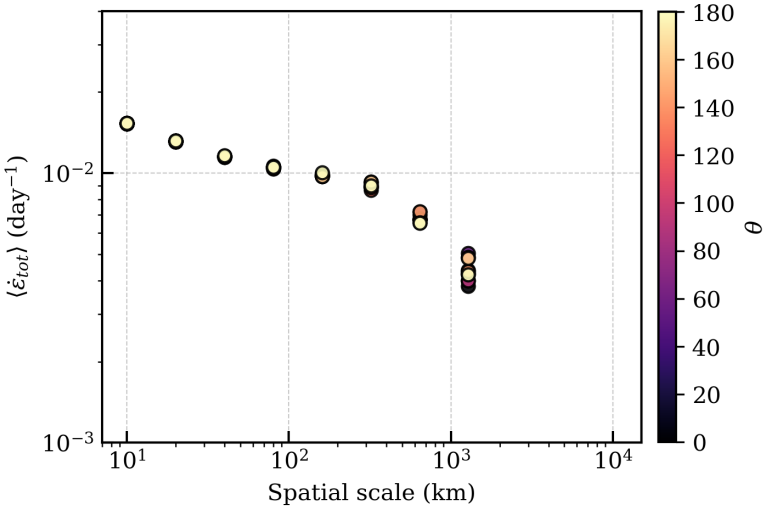

Figure 5. Scale dependence of RGPS (normalized) mean total strain rates for 29-31 January 2002, rotated with an angle θ.

https://doi.org/10.5194/egusphere-2026-2911
Preprint. Discussion started: 30 June 2026

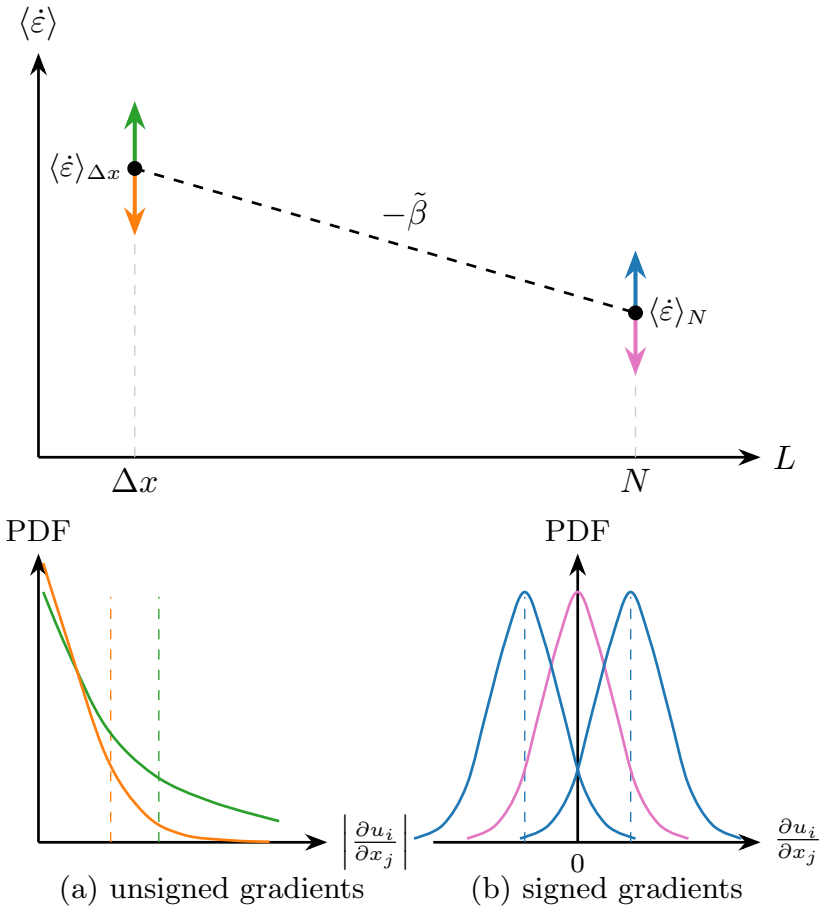

Figure 6. Schematic of the scaling exponent approximation $\tilde{\beta}$ and dependence on quantities derivable directly from the PDF of the deformation. In a winter-averaged RGPS and sea ice model ensemble, the two-point slope estimate $\tilde{\beta}$ is highly correlated with β (r = 0.92; Fig 7).

https://doi.org/10.5194/egusphere-2026-2911
Preprint. Discussion started: 30 June 2026

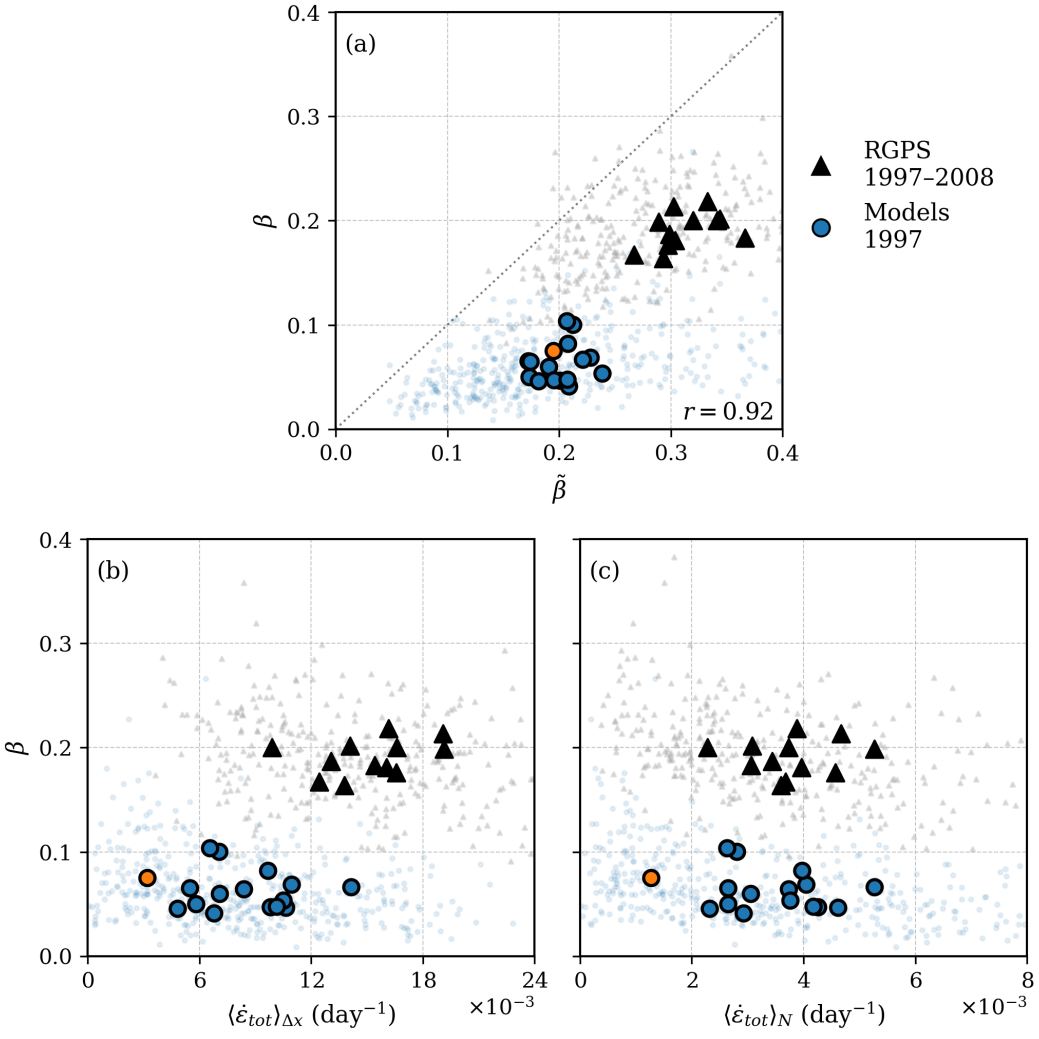

Figure 7. Correlation between the scaling exponent β (y-axis) and (a) the approximated scaling exponent $\tilde{\beta}$ (x-axis), (b) the deformation intensity $\langle \dot{\varepsilon}_{tot} \rangle_{\Delta x}$, and (c) the deformation mean $\langle \dot{\varepsilon}_{tot} \rangle_N$ of RGPS (black) and sea ice models (blue), except FESOM (4km; orange). A complete list of the models can be found in Fig. 11. The winter and model averages are shown in large symbols. A linear fit corresponding to the best fit for the winter averages between β and $\tilde{\beta}$ has a correlation of 0.92 and is not shown. The dotted line shows a 1:1 fit. Most data falls under this 1:1 line, meaning β is lower than $\tilde{\beta}$, coherent with known break of scaling at large scale. The models are mostly grouped together with lower β (and $\tilde{\beta}$) values than RGPS, and models have generally lower $\langle \dot{\varepsilon}_{tot} \rangle_{\Delta x}$ compared to RGPS, and similar $\langle \dot{\varepsilon}_{tot} \rangle_N$ values. Similar results are obtained using 2008 model outputs (not shown).

https://doi.org/10.5194/egusphere-2026-2911
Preprint. Discussion started: 30 June 2026

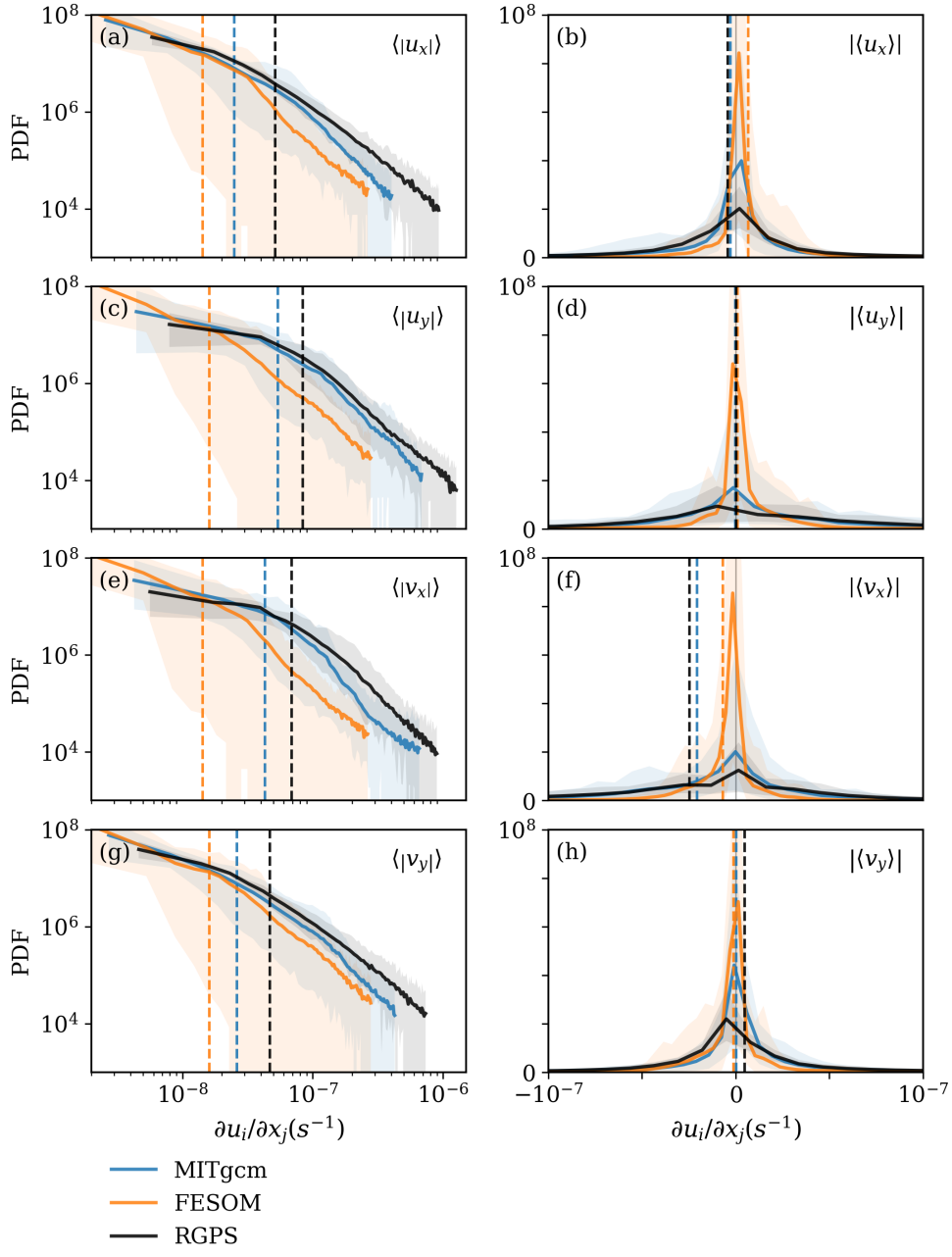

Figure 8. PDF of spatial mean of (a-c-e-g) the absolute value and (b-d-f-h) the signed values of velocity gradients ($\partial u/\partial x, \partial u/\partial y, \partial v/\partial x$, and $\partial v/\partial y$), for the winter 1997 of RGPS (black), MITgcm (2km; blue) and FESOM (4km; orange). The shading represents the 5th-95th percentile range across winters. The dashed lines show the mean values for each data set.

https://doi.org/10.5194/egusphere-2026-2911
Preprint. Discussion started: 30 June 2026

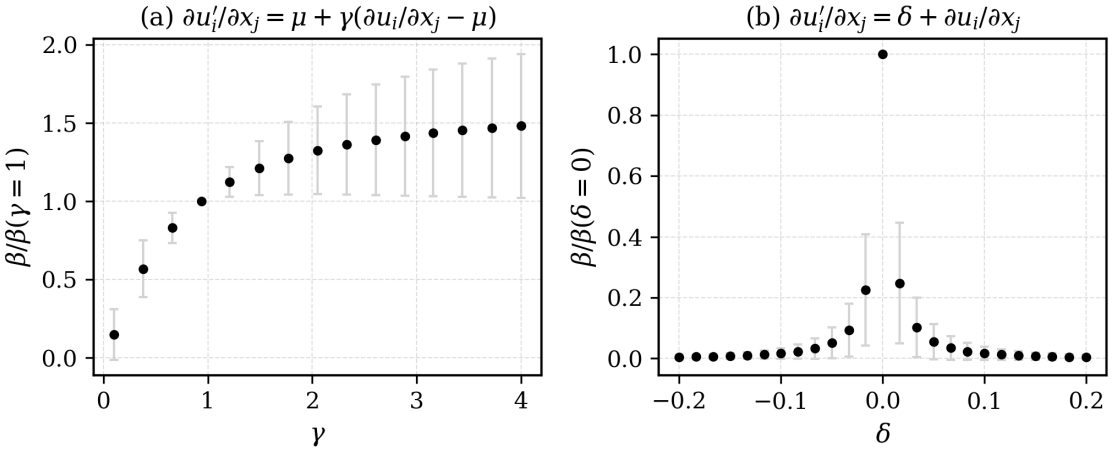

Figure 9. Scaling of RGPS (normalized) for 20 random snapshots as a function of (a) a multiplicative factor γ ($\mu = \overline{\partial u_i/\partial x_j}$) and (b) an additive factor δ on the velocity gradients. Symbols indicate the mean across the snapshots, while the error bars represent the standard deviation. The multiplicative perturbation modifies the deformation intensity ($\langle \dot{\varepsilon}_{tot} \rangle_{\Delta x}$), whereas the additive perturbation modifies the mean deformation ($\langle \dot{\varepsilon}_{tot} \rangle_N$), thereby acting as tuning parameters for β (see Fig. 6).

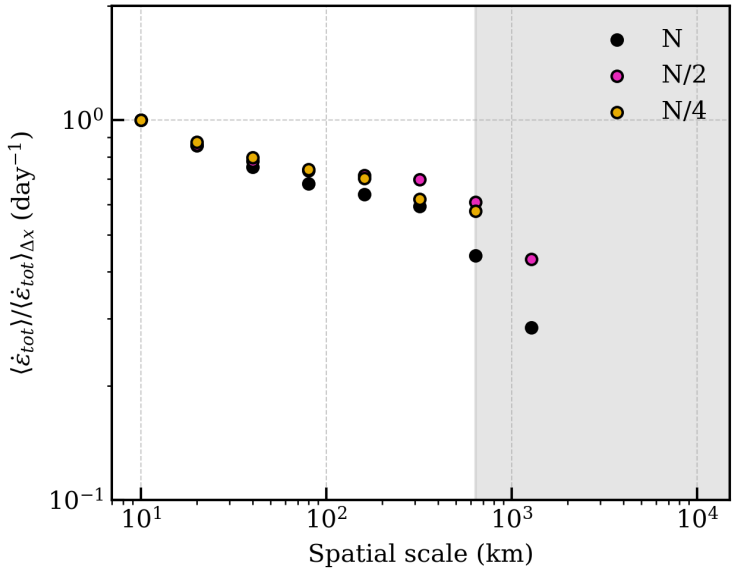

Figure 10. Scale dependence of RGPS (normalized) mean total strain rates for 29-31 January 2002 in the full (N), half field ($N/2$) and quarter field ($N/4$) physical domain, referenced to the centroid. The shading represents the scales at which there is strong departure from log-linear scaling, which is identical for all domain sizes. Note that the scaling ends at L=640 km for the smaller domain (yellow).

https://doi.org/10.5194/egusphere-2026-2911
Preprint. Discussion started: 30 June 2026

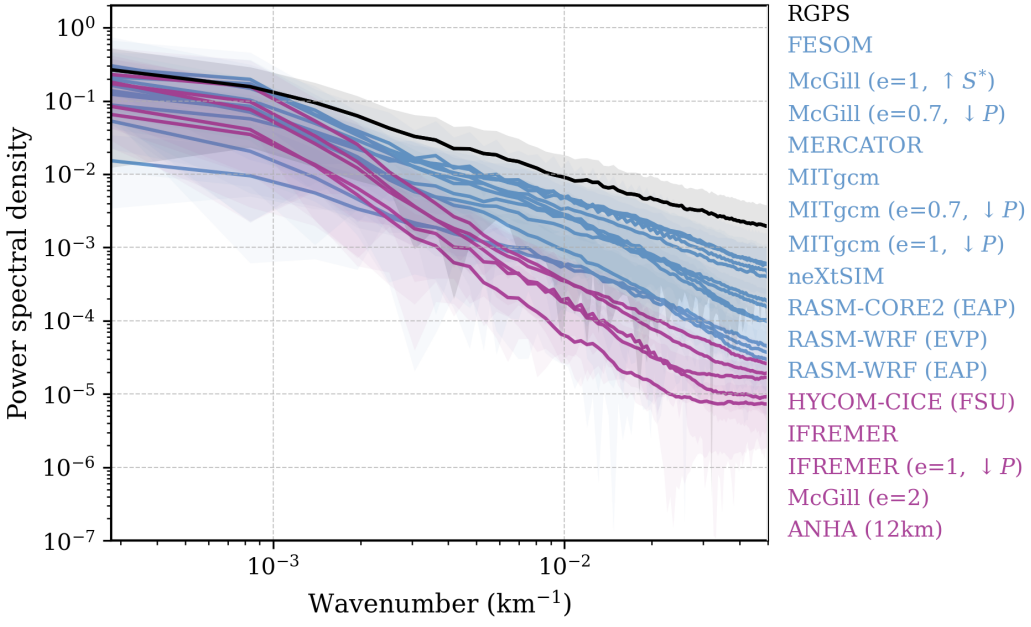

Figure 11. Spectral density of deformation for RGPS (black), models reproducing the observed spectral slope (blue), and models departing from it (purple) for the 1997 winter. The thick lines represent the time average and the shading represents one standard deviation across winters. Similar results are obtained for the 2008 winter (not shown). A Tukey window was applied to suppress boundary effects. Results shown are robust to the exact mask definition.